

# Dynamic guanidinium sulfate salt for selective carbon dioxide adsorption with negative pressure inflexion

Received: 24 August 2025

Accepted: 28 January 2026

Published online: 11 February 2026

Check for updates

Li Zhao<sup>1,3</sup>, Chengxi Zhao<sup>2,3</sup>, Congyan Liu<sup>1,3</sup>, Zhilin Xiang<sup>1</sup>, Chiran Wang<sup>1</sup>,  
Songlin Cui<sup>1</sup>, Linjiang Chen<sup>2</sup>✉ & Bo Liu<sup>1</sup>✉

Hydrogen bonds' flexible distances and moderate strength entitle compounds to dynamic properties under external stimuli. Here we report multiple phase transitions and counter-intuitive CO<sub>2</sub> adsorption behavior of dynamic guanidinium sulfate (GS) salt assembled via hydrogen-bonds. Exploration based on the energy landscape generated by crystal structure prediction (CSP) reveals three porous GS phases with stability of  $\alpha > \beta > \gamma$  and the inverse order of porosity, agreeing with experimental results. Transformations among polymorphs via heating or compressing involve ion rearrangement. Adsorption isotherms of  $\beta$ -GS indicate that CO<sub>2</sub> firstly enters the isolated cavities at a low gating pressure, and further increasing CO<sub>2</sub> pressure leads to the continuous gas uptake but reduced pressure at a critical point and thus an unexpected negative pressure inflexion (NPI), followed by the final adsorption saturation. Theoretical calculations demonstrate that the NPI behavior stemmed from the GS structural transition from  $\beta$  to more porous  $\gamma$ -phase, with the  $\gamma$ -GS phase becoming more energy-favorable as CO<sub>2</sub> uptake increases. Specific supramolecular interactions ensure CO<sub>2</sub> selectivity and easy regeneration. With a CO<sub>2</sub> uptake of 4.2 mmol g<sup>-1</sup> (273 K, 100 kPa), GS salt exhibits great promise for CO<sub>2</sub> capture and transport, demonstrating the potential of simple hydrogen-bonded salts as adaptive materials.

Gas adsorption isotherms have long served as essential tools for characterizing porous materials. Their shapes are traditionally interpreted based on the static structural features of rigid adsorbents, including pore size distribution, specific surface area, and surface chemistry. Microporous materials bearing rigid pores display a typical type I adsorption isotherm<sup>1</sup> (Fig. 1a). However, this conventional understanding becomes inadequate when applied to dynamic sorbents that undergo structural transformations upon guest molecule uptake. In such systems, adsorption behavior reflects not only pre-existing porosity but is also significantly governed by kinetic processes driven by adsorption-induced structural changes. These processes

frequently lead to distinctive isotherm features such as multi-step profiles, pronounced hysteresis, and unusual inflection points, which often indicate selective gas uptake mediated through framework flexibility or phase transitions. Adsorbents having flexible, adaptive, or dynamic pores/channels or discrete cavities exhibit stepped or S-shaped adsorption isotherms (Fig. 1b), providing significant advantages for practical adsorption and separation owing to the increased working capacity<sup>2,3</sup>. The abrupt change in gas uptake reflected by a steep profile in the isotherm is a signature of a gating effect, which involves a structural transition of the adsorbent driven by guest adsorption. A counter-intuitive phenomenon of negative gas

<sup>1</sup>Hefei National Laboratory for Physical Sciences at the Microscale, School of Chemistry and Materials, University of Science and Technology of China, Hefei, Anhui, China. <sup>2</sup>State Key Laboratory of Precision and Intelligent Chemistry, University of Science and Technology of China, Hefei, Anhui, China. <sup>3</sup>These authors contributed equally: Li Zhao, Chengxi Zhao, Congyan Liu. ✉ e-mail: [linjiangchen@ustc.edu.cn](mailto:linjiangchen@ustc.edu.cn); [liuchem@ustc.edu.cn](mailto:liuchem@ustc.edu.cn)

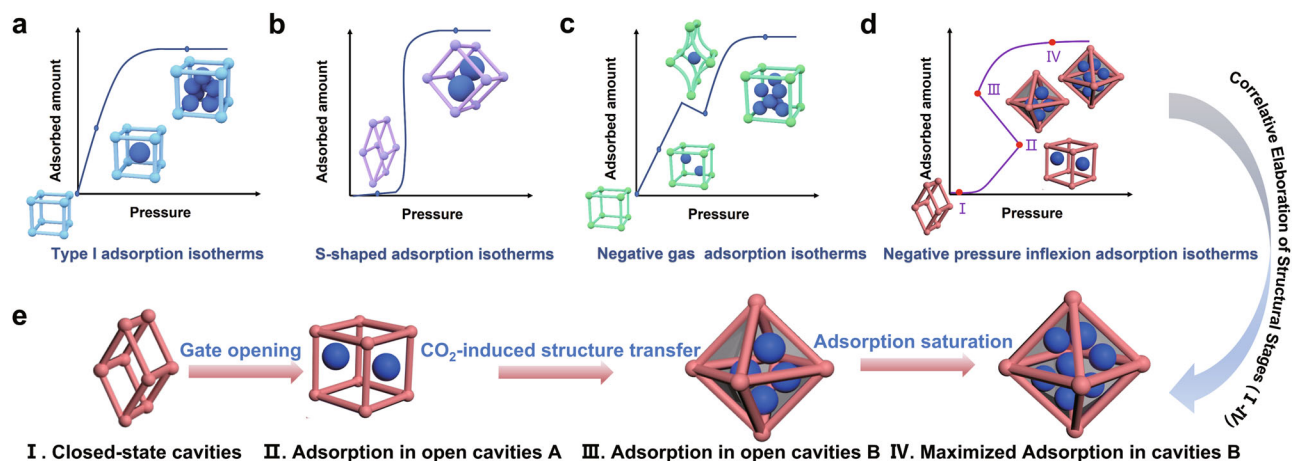


**Fig. 1 | The relationship between the adsorption isotherm and the adsorbent structure.** **a** Type I adsorption isotherm and rigid microporous materials. **b** S-shaped adsorption isotherm and flexible porous materials. **c** Negative gas

adsorption isotherm associated with structural deformation and pore contraction of adsorbents. **d, e** Negative pressure inflexion adsorption isotherm and structural changes of the adsorbent with increasing gas pressure.

adsorption in a stepped isotherm on DUT-49 (Dresden University of Technology No. 49) has been identified<sup>4</sup>. The process involves pressure-induced structural deformation and pore contraction with gas desorption during pressure increase, resulting in pressure amplification in a microsystem (Fig. 1c). In contrast to Negative Gas Adsorption (NGA), we identify and define a distinct phenomenon, which we term Negative Pressure Intrusion (NPI), observed in a dynamic porous framework (Fig. 1d). The NPI event is initiated by a guest-induced structural transition that triggers a substantial and abrupt increase in the material's gas adsorption capacity. Within a constant-volume system, this surge in uptake causes a net depletion of gas molecules from the free gas phase, resulting in a characteristic pressure decrease. Consequently, although both NGA and NPI produce anomalous steps in adsorption isotherms driven by structural transitions, they represent fundamentally opposite mechanisms. While the dynamic sorption properties of flexible metal-organic frameworks (MOFs) and covalent organic frameworks (COFs) have been extensively studied, hydrogen-bonded frameworks (HOFs) are emerging as a promising alternative<sup>5-7</sup>. Certain HOFs exhibit permanent porosity, enabling applications in gas adsorption and separation<sup>8-10</sup>. However, the construction of robust HOFs remains challenging due to the weak nature of hydrogen bonds<sup>5,11</sup>. A key strategy to overcome this limitation involves incorporating electrostatic interactions through charge-assisted hydrogen bonds, leading to a subclass known as hydrogen-bonded ionic frameworks (HIFs). Comprising ionic building units, HIFs benefit from enhanced structural stability imparted by these stronger interactions, without compromising the intrinsic flexibility derived from the versatile geometry of hydrogen bonds<sup>12</sup>. This flexibility allows HIFs to undergo reversible structural reorganization in response to external stimuli such as pressure, heat, or solvent<sup>13-16</sup>. The dynamic behavior of HIFs has been demonstrated in several systems. For example, one HIF constructed from guanidinium cations and methyl borate anions undergoes a reversible collapse and reconstruction process to capture and release methanol molecules<sup>17</sup>. Similarly, another HIF based on  $[\text{Co}(\text{NH}_3)_6]^{3+}$  and  $\text{SO}_4^{2-}$  ions shows reversible framework disassembly and reassembly, facilitating low-energy  $\text{CO}_2$  capture and release<sup>15</sup>.

Here, we report three phases of guanidinium sulfate (GS) as a model HIF system, designated  $\alpha$ -,  $\beta$ -, and  $\gamma$ -GS based on their thermodynamic stability as revealed by the complete energy landscape from crystal structure prediction (CSP). Under mild conditions, GS shows great potential for  $\text{CO}_2$  capture, storage and transport, with an uptake capability of up to  $4.2 \text{ mmol g}^{-1}$  at 273 K and 100 kPa, an uptake

that is competitive with leading MOFs and HOFs and other leading porous materials. Impressively, we observed that this exceptional performance is attributed to a multi-stepped  $\text{CO}_2$  adsorption process exhibited by  $\beta$ -GS, which displays an abnormal negative pressure inflexion (NPI) phenomenon under near-ambient conditions. As demonstrated in Fig. 1d,  $\beta$ -GS is inactive toward  $\text{CO}_2$  adsorption at low pressures. With increasing  $\text{CO}_2$  pressure, the gas overcomes an energy barrier and infiltrates the isolated cavities of the GS structure until a critical pressure is reached. Subsequent  $\text{CO}_2$  dosing leads to continuous gas uptake accompanied by a pressure decrease in the test tube, resulting in a negative pressure inflexion in the adsorption isotherm, followed by complete saturation and a phase transformation from  $\beta$ -GS to  $\gamma$ -GS (Fig. 1e). We note that apparent pressure inflexions in the adsorption isotherms of some MOFs have been reported and mechanistically investigated. Building upon these fundamental insights, the present study provides a more comprehensive mechanistic interpretation<sup>6,18-23</sup>. The NPI adsorption in H-bonded salt and HOF materials has not been reported, to the best of our knowledge. Note that the  $\text{CO}_2$ -induced crystallization of  $\text{CO}_2@GS$  clathrate from GS aqueous solution in our previous work is a typical supramolecular assembly process that is similar to the formation of natural gas hydrates and hence inherently distinct from  $\text{CO}_2$  adsorption and diffusion in the solid salt<sup>24</sup>.

## Results

### Structure and porosity of $\alpha$ -GS

$\alpha$ -GS is directly prepared by neutralization reaction between commercially available guanidinium carboxylate and sulfuric acid and recrystallized from aqueous solution<sup>24</sup>. As the parent compound of guanidinium organosulfonate compounds<sup>25</sup>,  $\alpha$ -GS is assembled through N-H...O H-bonds between  $\text{Gua}^+$  ions and  $\text{SO}_4^{2-}$  ions<sup>26</sup> (Supplementary Fig. 1a-c). Detailed structural analyses disclose that  $\alpha$ -GS contains isolated cavities, which are situated in the ionic cages composed of  $\text{SO}_4^{2-}$  ions and  $\text{Gua}^+$  ions connected by H-bonds (Supplementary Fig. 1d). With a probe radius of 1.4 Å, the cavity volume within a single unit cell was found to be  $750.22 \text{ \AA}^3$ , accounting for 13.4% of the unit cell volume. Thermogravimetric analysis (TGA) of  $\alpha$ -GS manifests that there is no weight loss before its decomposition temperature at 545 K, indicating there is no crystalline water in  $\alpha$ -GS (Supplementary Fig. 2).  $\alpha$ -GS activated at 353 K displays negligible  $\text{N}_2$  adsorption at 77 K (Supplementary Fig. 3), but a reasonable  $\text{CO}_2$  adsorption of  $0.58 \text{ mmol g}^{-1}$  at 100 kPa and 273 K (Fig. 2a, equilibration time of 600 s), suggesting that  $\alpha$ -GS can selectively adsorb carbon dioxide.

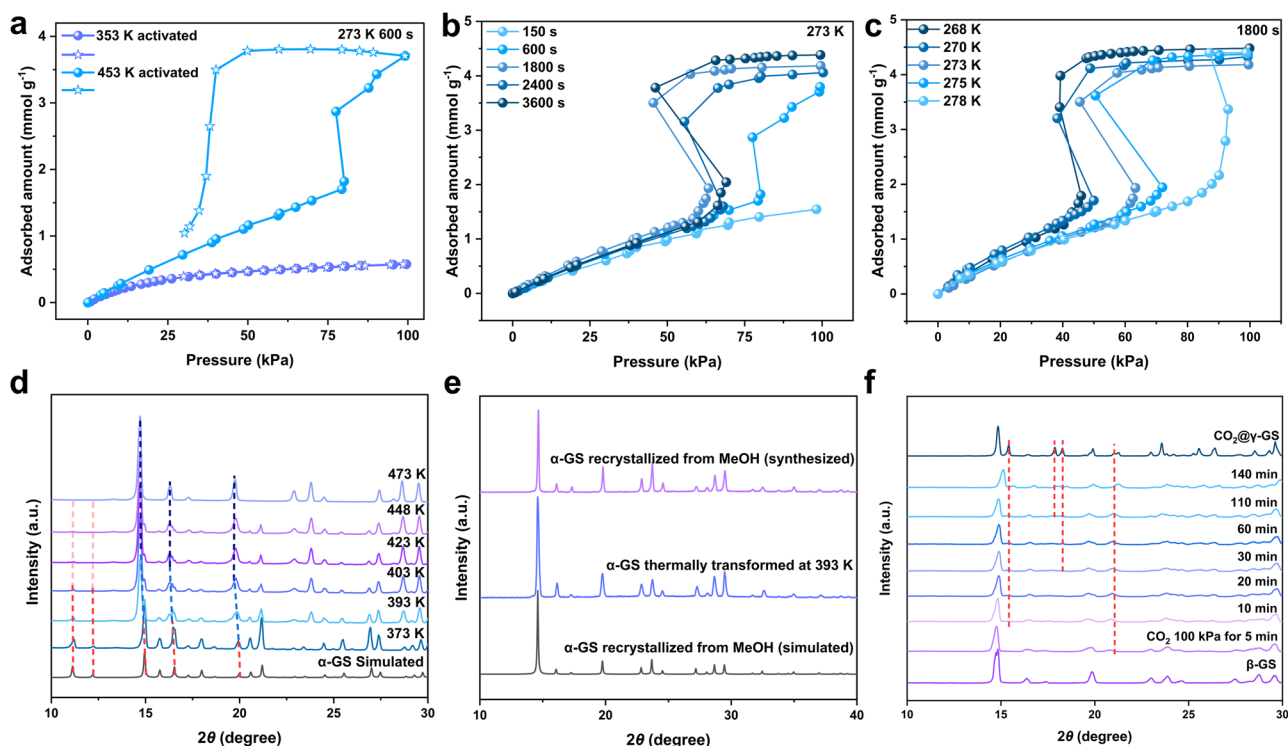


**Fig. 2 | CO<sub>2</sub> adsorption isotherms of GS and corresponding structural changes.**

**a** CO<sub>2</sub> adsorption and desorption isotherms of  $\alpha$ -GS activated at 353 K and 453 K under vacuum, respectively, at 273 K with an equilibrium time of 600 s. **b** CO<sub>2</sub> sorption isotherms of  $\alpha$ -GS activated at 453 K with various equilibration conditions at 273 K. **c** The CO<sub>2</sub> adsorption isotherms of  $\alpha$ -GS activated at 453 K at various temperatures with equilibration time of 1800 s. **d** Variable-temperature powder X-ray diffraction (VT-PXRD) patterns of  $\alpha$ -GS recorded from 373 to 473 K. The red dashed lines highlight the shift and disappearance of characteristic peaks

corresponding to the  $\alpha$  phase, while the blue dashed lines indicate the  $\beta$  phase. **e** Powder X-ray diffraction (PXRD) patterns of  $\alpha$ -GS were collected for three distinct states: simulated patterns based on single-crystal X-ray diffraction (SCXRD) data of methanol (MeOH)-recrystallized samples, thermally transformed phases at 393 K, and experimentally obtained MeOH-recrystallized samples. **f** In situ PXRD patterns monitoring the phase transition from  $\beta$ -GS to CO<sub>2</sub>@ $\gamma$ -GS under 100 kPa CO<sub>2</sub> at varying exposure times of 278 K (The red dashed lines indicate the emerging diffraction peaks corresponding to CO<sub>2</sub>@ $\gamma$ -GS).

The scanning electron microscope (SEM) image shows that the sizes of GS particles used for adsorption measurement are on the micrometer scale (Supplementary Fig. 4), ensuring that surface adsorption effects are excluded.

### Abnormal CO<sub>2</sub> adsorption isotherm of GS

Abnormal CO<sub>2</sub> adsorption behavior with a pronounced hysteresis phenomenon was observed when  $\alpha$ -GS is activated at 453 K under vacuum (Fig. 2a–c). For typical isotherm measurements of porous materials, equilibration conditions for each data point are set as pressure fluctuation lower than  $\pm 1\%$  within 150 s. Upon extending the equilibrium time to 600 s, the CO<sub>2</sub> adsorption amount is increased to 3.8 mmol g<sup>-1</sup> (Fig. 2a). Unexpectedly, the amount of adsorbed CO<sub>2</sub> continues to rise during the desorption stage, which suggests that equilibrium had not been reached by the end of adsorption at 100 kPa and the CO<sub>2</sub> adsorption continues even at the lowering pressure during the desorption process. Specifically, during the initial desorption stage in the pressure range of 70–100 kPa, the adsorbed amount exceeds the value recorded at the end of the adsorption branch at the same pressure. This phenomenon was not observed in  $\alpha$ -GS activated at 353 K under identical measurement conditions with a 600 s equilibrium time (Fig. 2a). We attribute this behavior to the sluggish kinetics of the structural transformation in the 453 K-activated sample. Subsequently, we further prolonged the equilibrium time to 1800–3600 s to ensure adsorption equilibrium (Fig. 2b, see experimental details in “Methods”). Then an odd multi-stepped adsorption isotherm with a negative pressure inflexion (NPI) was observed (Fig. 2b). We repeated measurements to exclude the experimental errors, and the phenomenon was reproducible (Supplementary Figs. 5, 6). After carefully

analyzing the adsorption isotherm in the low-pressure range, we found that CO<sub>2</sub> adsorption below 1 kPa was negligible, indicating a gating effect (gating point) (Supplementary Fig. 8b). Subsequently, CO<sub>2</sub> uptake displayed an approximately linear relationship with pressure increasing up to 63 kPa at 273 K (critical point). Below the critical pressure, the adsorption data obtained with 600 s and 1800 s equilibration times were coincident (Supplementary Fig. 7). With continuous pressure increase, the NPI phenomenon emerged, accompanied by a sudden increase in CO<sub>2</sub> uptake but a sharp pressure decrease inside the sample cell, showing an anomalous pressure drop to 45 kPa (NPI point), until final adsorption saturation is reached. The isotherm shows an obvious hysteresis loop, where desorption starts when the pressure drops below 50 kPa at 273 K (Supplementary Fig. 8a).

The CO<sub>2</sub> adsorption isotherms for the sample of  $\alpha$ -GS activated at 453 K at various temperatures were collected with an equilibrium time of 1800 s (Fig. 2c, Supplementary Figs. 8–12). Multi-stepped adsorption isotherms with NPI phenomena are observed at temperature ranging from 268 to 278 K (Fig. 2c). Once the temperature exceeds 278 K, prolonged equilibrium time setting does not change the sorption behavior of GS in the pressure range of 0 to 100 kPa and the desorption closely overlap the adsorption process, without hysteresis loop (Supplementary Fig. 13). We note that the shape of the adsorption isotherm before critical point at 273 K is similar to that at 298 K (Supplementary Fig. 14). To exclude the influence of adsorption equilibrium time, we further performed adsorption measurements on  $\alpha$ -GS activated under 353 K with an extended equilibration period (Supplementary Fig. 15), which displayed a normal adsorption isotherm without gating effect and NPI phenomenon at pressures below 100 kPa at 273 K.

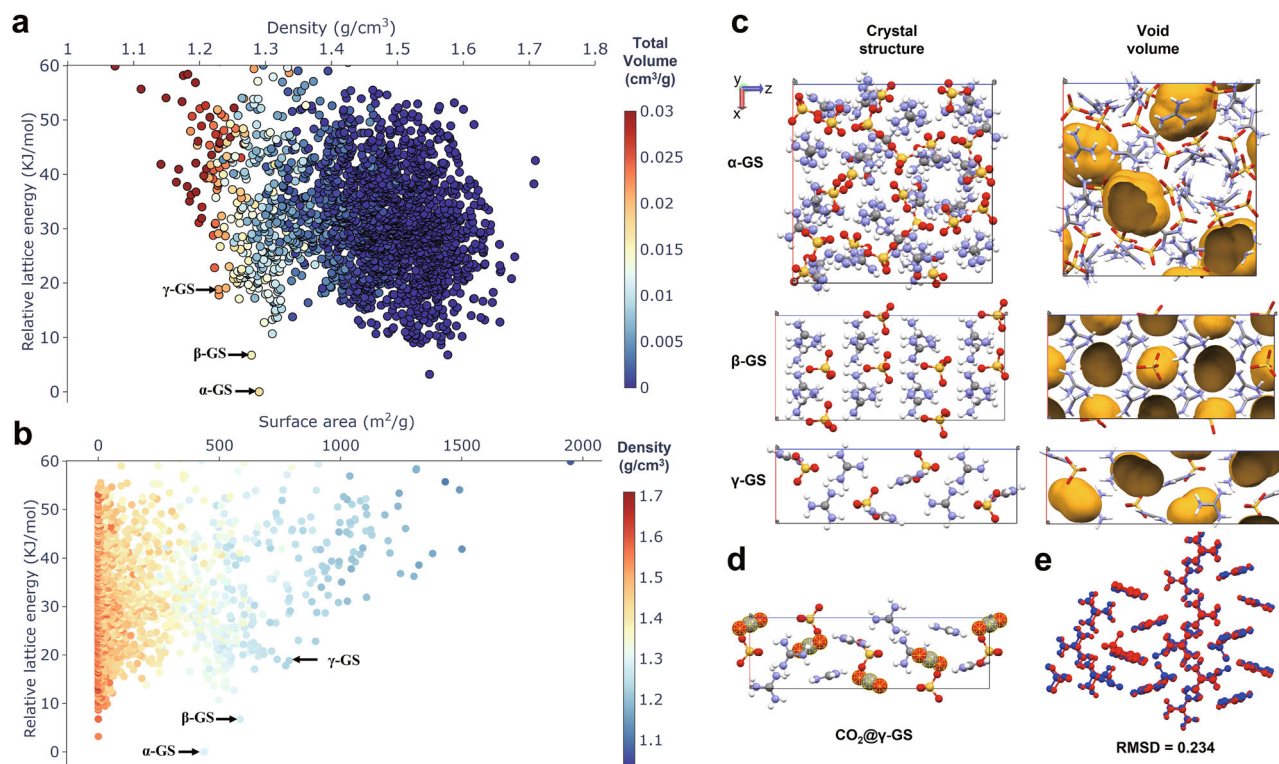


**Fig. 3 | Exploring the energy landscape of GS polymorphs. a** Energy–structure–function map for GS plotted against crystal density and color-coded by total volume. **b** Energy–structure–function map for GS plotted against total surface area and color-coded by density. **c** Crystal structures of the  $\alpha$ -GS,  $\beta$ -GS, and  $\gamma$ -GS phases, with their corresponding void volumes. The probe radius used here is set to 1.65 Å,

and the contact surface is used for visualization. **d** Crystal structures of  $\text{CO}_2@ \gamma$ -GS, with the corresponding  $\text{CO}_2$  positions highlighted using the space-filled display method. The  $\text{CO}_2$  positions are consistent with the pores in the  $\gamma$ -GS. **e** Overlay of the predicted  $\gamma$ -GS (theoretical) and the  $\text{CO}_2$ -adopted  $\text{CO}_2@ \gamma$ -GS (experimental). The smallest molecules ( $\text{CO}_2$ ) are ignored during packing similarity testing.

To elucidate the unconventional  $\text{CO}_2$  adsorption behavior, we conducted PXRD analyses for  $\alpha$ -GS sample activated at 453 K and found a different crystalline phase (Supplementary Fig. 16). The in situ PXRD patterns during heating  $\alpha$ -GS sample from 373 to 473 K also disclosed the phase transition starting from 393 K (Fig. 2d). The results are consistent with differential scanning calorimetry (DSC) data, which indicate a structural transformation initiating at 393 K and reverting at 261 K (Supplementary Fig. 17). Fortunately, the single crystals were obtained by dissolving  $\alpha$ -GS powder in methanol and allowing the solution to stand undisturbed at room temperature for 7 days. The crystal structure was subsequently determined by single-crystal X-ray diffraction (Supplementary Table 2). The simulated PXRD patterns exactly overlap with the patterns obtained from thermal transformation of  $\alpha$ -GS (Fig. 2e, Supplementary Fig. 18). This confirms that the same  $\beta$ -GS structure is produced via both solid-state thermal transformation and solution-phase recrystallization. Herein, we denote the new structure as the  $\beta$ -GS phase. In the  $\beta$ -GS structure, the  $\text{SO}_4^{2-}$  anions are disordered over two equivalent positions, forming charge-assisted hydrogen bonds (Supplementary Fig. 19a, b) with surrounding  $\text{Gua}^+$  cations. The connectivity pattern generates a three-dimensional framework as illustrated in Supplementary Fig. 19c, d. Similar to  $\alpha$ -GS, isolated cavities are also present in  $\beta$ -GS. The cavity volume within a single unit cell was determined to be  $433.90 \text{ \AA}^3$  using a probe radius of 1.4 Å, accounting for 18.7% of the unit cell volume.

To further understand the adsorption and the associated structural transition mechanism, we collected the PXRD patterns before and after critical pressure (Supplementary Fig. 20) and identified another phase after the critical pressure, while the  $\beta$ -GS structure persisted below this threshold. We further performed in situ PXRD measurements over  $\beta$ -GS sample under  $\text{CO}_2$  pressure of 100 kPa at 278 K and

observed the same new phase (Fig. 2f). Notably, the PXRD patterns of the new phase exhibited complete consistency with the one simulated from  $\text{CO}_2@ \text{GS}$  structure that was reported in our previous work<sup>24</sup> (Supplementary Fig. 21). Thereafter, we named the new phase as  $\gamma$ -GS. However, efforts to grow  $\text{CO}_2$ -free  $\gamma$ -GS single crystals were unsuccessful, both through optimizing crystallization conditions and activating  $\text{CO}_2@ \gamma$ -GS. Though we obtained the structural information of GS under different conditions, it is still challenging to understand the phase transition events among the GS phases, especially during the  $\text{CO}_2$  adsorption process; therefore, we resort to computational calculations to disclose the transition mechanism, as discussed as follows.

### Exploration of the crystal structure energy landscape of GS

Multistep adsorption isotherms may arise from guest-induced polymorphic transitions<sup>27,28</sup> (although other mechanisms, such as stepwise site filling, can produce similar features). Accordingly, we performed crystal structure prediction (CSP) to systematically map the high-dimensional potential energy surface and establish the relative stabilities of polymorphs, thereby providing mechanistic insight into the system. During the CSP process, hundreds of thousands of trial structures were generated and subsequently optimized geometrically using a force field (Supplementary Fig. 22). Duplicates were then removed, and the low-energy structures were selected for further optimization at the DFT level, alongside the single crystal structures obtained from experiments (Fig. 3, see details in “Methods”).

The CSP landscape for GS is markedly different from typical organic systems, because the global minimum ( $\alpha$ -GS) is a porous crystal (Fig. 3a–c), even though the GS building unit itself does not possess an inherent intramolecular cavity, unlike classic cage-like or macrocyclic porous molecules. This landscape indicates that the  $\alpha$ -GS

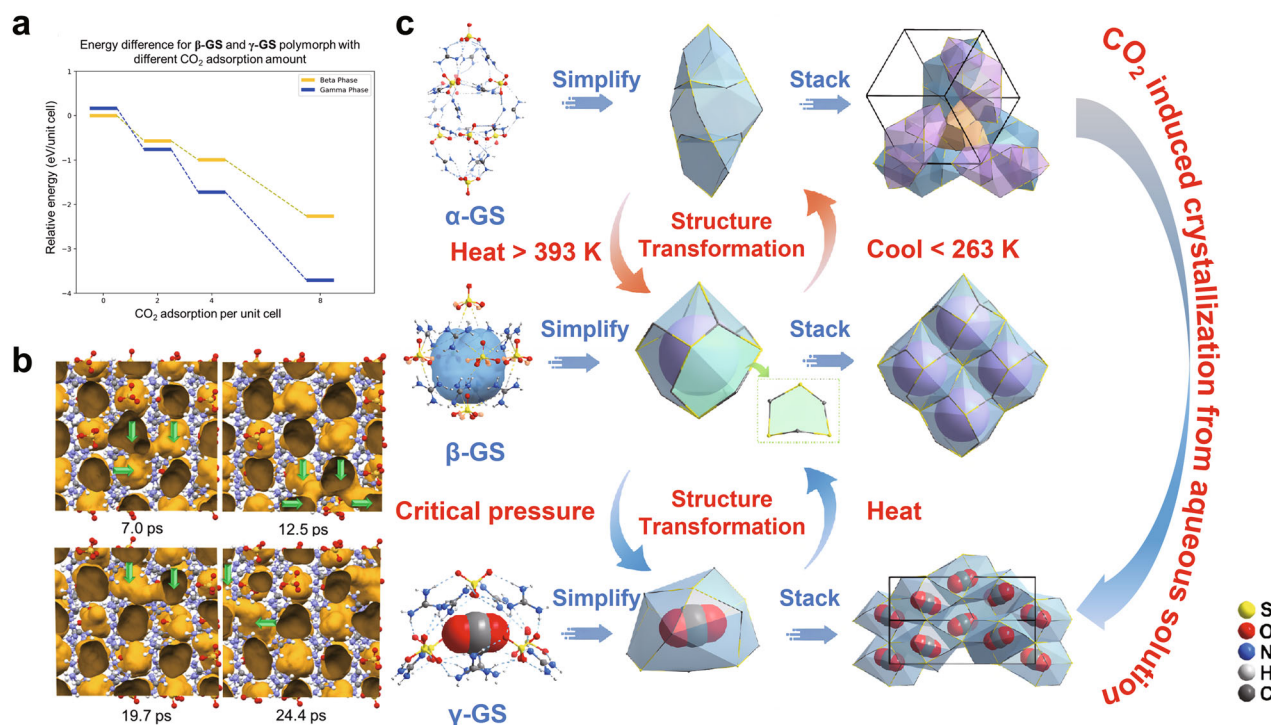


**Fig. 4 | Structural transformation and phase transition among  $\alpha$ -GS,  $\beta$ -GS and  $\gamma$ -GS.** **a** DFT calculation results of the potential energy difference between the beta and gamma phase polymorphs with different CO<sub>2</sub> adsorption ratios. **b** Pore breathing events during MD simulations. The initially separated pockets gradually

open and either connect to each other or become closed over time. Connected pockets are indicated by green arrows in the figure. A probe radius of 1.2 Å was used in this analysis. **c** Structural transformation and phase transition of GS under different conditions.

crystal is the most thermodynamically stable polymorph.  $\beta$ -GS, which is 6.76 kJ mol<sup>-1</sup> higher in energy than the global minimum, falls within the typical energy window for the appearance of polymorphs in experiments<sup>29</sup>. In the lower-density region of the energy landscape,  $\gamma$ -GS was identified with a relative energy of 18.82 kJ mol<sup>-1</sup>, and its backbone perfectly matched that of CO<sub>2</sub>@ $\gamma$ -GS (Fig. 3d, e). The high relative energy for such a small molecule system suggests that this crystal structure may be challenging to be accessed under normal experimental conditions. This may explain why pure  $\gamma$ -GS crystals have not yet been obtained in experiments. The high-dimensional energy surface, projected onto the structural parameter of surface area, is also shown in Fig. 3b. In this plot, it is clear that  $\alpha$ -GS,  $\beta$ -GS, and  $\gamma$ -GS are all situated on the leading edge and appear on separate spikes, indicating that they reside in distinct energy basins<sup>30,31</sup>. All of them exhibit porous properties, as illustrated in Fig. 3c. Moreover, a densely packed structure with a density of 1.55 g cm<sup>-3</sup> and a relative energy of 3.19 kJ mol<sup>-1</sup> was also identified in the landscape, suggesting that this system may possess additional potential structures yet to be observed experimentally (Supplementary Fig. 23). CSP results reveal three GS phases with stability of  $\alpha > \beta > \gamma$  and the inverse order of porosity, agreeing with our experimental data. However, CO<sub>2</sub> adsorption can alter the relative energy ranking and induce a structural transition, which is associated with the abnormal NPI phenomenon observed in this system.

### GS structural transformation

We further performed the density functional theory calculations to investigate the phase transition during the CO<sub>2</sub> adsorption process. To eliminate the structural disorder in  $\beta$ -GS, several non-disordered crystal models were manually constructed, and the one with the lowest lattice energy after structural relaxation was selected for further analysis. For a meaningful comparison, the symmetry of  $\gamma$ -GS was constrained to the  $C4_122_1$ , giving it the same pore count and the same

number of molecules per unit cell as  $\beta$ -GS (Supplementary Table 3). Models of both polymorphs were then constructed at a series of CO<sub>2</sub> loadings, and their relaxed lattice energies were compared (Fig. 4a). In the guest-free state,  $\beta$ -GS is more stable than  $\gamma$ -GS, in agreement with the CSP result. However, the energy difference between CO<sub>2</sub>@ $\beta$ -GS and CO<sub>2</sub>@ $\gamma$ -GS diminishes rapidly with increasing CO<sub>2</sub> uptake and inverts. The energy difference rises to 1.44 eV per unit cell when the pores of both polymorphs are fully saturated, providing the thermodynamic driving force for the observed phase transition during the CO<sub>2</sub> adsorption process. These computational results support that  $\gamma$ -GS is a distinct thermodynamic phase, not merely a configurational variant of  $\beta$ -GS.  $\gamma$ -GS is more porous than  $\beta$ -GS as illustrated by CSP (cf. Specific surface area: 787.6 versus 585.4 m<sup>2</sup> g<sup>-1</sup>, and void volume: 0.02145 versus 0.01595 mm<sup>3</sup> g<sup>-1</sup>), therefore, the transition from  $\beta$ - to  $\gamma$ -GS at critical pressure point gives rise to the sharp CO<sub>2</sub> adsorption and sudden pressure drop in the test tube, namely NPI (negative pressure inflexion) event in adsorption isotherm as observed in Fig. 2b, c.

As shown in Fig. 3c, void space analysis indicates that  $\beta$ -GS contains isolated, unconnected pores. While CO<sub>2</sub> adsorption appears limited from a static perspective due to restricted guest diffusion, a dynamic view is required to capture the full behavior. Modeling diffusion-driven polymorphic transitions remains challenging, as such rare events occur on timescales beyond those accessible to conventional Molecular dynamics (MD) simulations. To explore potential pore-breathing behavior, MD simulations were performed on pure  $\beta$ -GS. Although no continuous channels were observed using a probe radius of 1.65 Å, transient channels appeared between occluded sites when a smaller probe radius of 1.2 Å was used, temporarily connecting adjacent voids (Fig. 4b). These pore-breathing events are attributed to the flexibility of the hydrogen-bond network<sup>32</sup> (Supplementary Fig. 24). The complete CO<sub>2</sub>-induced phase transformation from  $\beta$ -GS to  $\gamma$ -GS was experimentally observed to require over 5 h (Supplementary Fig. 25)—a time scale notably longer than the 1800 s

equilibration criterion employed in our adsorption measurements. Importantly, this extended transformation time does not conflict with the established equilibrium setting, where the system was considered to reach equilibrium only when the adsorbed amount varied within  $\pm 1\%$  over 1800 s. The observed slow kinetics originates from the coupled effects of restricted diffusion through transient channels and the rate-limiting solid-state structural rearrangement, with the phase transformation representing the primary kinetic bottleneck.

According to the above experimental data, we could delineate the phase transformation map of guanidinium sulfate under external stimuli. As shown in Fig. 4c,  $\alpha$ -GS is considered to be the thermostable phase, as revealed from the theoretical energy landscape.  $\beta$ -GS can be prepared via dissolving  $\alpha$ -GS powder in methanol or obtained by heating  $\alpha$ -GS to a temperature higher than 393 K, and  $\beta$ -GS is reversibly converted into  $\alpha$ -GS via cooling at a temperature lower than 263 K.  $\gamma$ -GS, as a high-energy phase, can't be produced in its pure phase under ambient conditions. Instead,  $\gamma$ -GS could exist as  $\text{CO}_2$  clathrate ( $\text{CO}_2@ \gamma$ -GS), via  $\text{CO}_2$  adsorption in  $\beta$ -GS beyond a critical pressure or directly  $\text{CO}_2$ -induced crystallization from GS aqueous solution, because the specific supramolecular interaction between  $\text{CO}_2$  and guanidinium ions stabilizes the  $\gamma$ -GS phase<sup>24</sup>.

### GS for $\text{CO}_2$ capture and storage

Although  $\text{CO}_2@ \gamma$ -GS readily releases  $\text{CO}_2$  at ambient conditions, the decomposition process is retarded by the presence of decomposed GS on the surface. The TG analysis of  $\text{CO}_2@ \gamma$ -GS showed a 17% weight loss prior to 353 K, ascribed to  $\text{CO}_2$  release (Supplementary Fig. 26). This aligns with the theoretical weight densities of  $\text{CO}_2$  in  $\text{CO}_2@ \gamma$ -GS (17 wt %), and agrees with the saturated  $\text{CO}_2$  adsorption amount ( $4.2 \text{ mmol g}^{-1}$ ). In contrast to desorbing  $\text{CO}_2$  from a 5–10 wt% organic-amine aqueous solution—a process plagued by the high thermal energy demand of heating water (due to its high heat capacity)—direct heating of the GS solid proves a significantly more energy-efficient way for the adsorbent's regeneration<sup>33</sup>. When a sealed reactor containing  $\beta$ -GS solid is charged with  $\text{CO}_2$  to 100 kPa at 273 K, a pressure decrease from  $\text{CO}_2$  adsorption is observed immediately, with an approximate equilibrium time of 60 min. Upon heating the reactor at 373 K,  $\text{CO}_2$  is released, and the pressure recovers. The pressure exceeds the initial value owing to the heating effect (Supplementary Fig. 27a). In the control experiment using NaCl replacing the  $\beta$ -GS solid, there is no observed pressure drop and heating at 373 K results in a pressure increase at the same scale raised from the heating effect. The results reveal that  $\text{CO}_2$  uptake and release are highly reversible over multiple cycles. Ten cycles of uptake/release display no performance decay (Supplementary Fig. 27b) and PXRD patterns of the  $\beta$ -GS adsorbent after the cycling tests align with those of the pristine  $\beta$ -GS (Supplementary Fig. 27c), confirming the stability of the  $\beta$ -GS.

A challenge associated with conventional gating effect in porous materials is the difficulty in preventing other gas species to enter the pores following the pore-opening triggered by the target molecule<sup>33,34</sup>.  $\beta$ -GS exhibits a unique selectivity for  $\text{CO}_2$  even in the presence of high-concentration  $\text{N}_2$ . When we subjected GS to a mixture gas of 70%  $\text{N}_2$  and 30%  $\text{CO}_2$  at 330 kPa ( $\text{CO}_2$  partial pressure of 100 kPa) and 273 K, there was negligible  $\text{N}_2$  adsorption under the experimental conditions detected by gas chromatography (GC) (See details in "Methods"). It is worth noting that  $\text{CO}_2$  adsorption by GS differs from physisorption in porous materials, including flexible MOFs, as physisorption typically doesn't change the connections between the frameworks<sup>35,36</sup>. And the adsorption is clearly not a chemisorption process, because there is no formation of new chemical bonds. Instead, it follows a supramolecular adsorption mechanism via the formation of clathrate compounds. In the process,  $\text{CO}_2$  uptake needs to overcome the energy barrier driven by pressure stimuli for lattice rearrangement of the GS crystal.

## Discussion

Guanidinium sulfate, as a hydrogen-bonded salt, exhibits multiple phase transformations owing to the dynamic and flexible attributes of H-bonds. We reveal three phases of guanidinium sulfate and further illustrate their transformation mechanism. Specifically, we discover a counter-intuitive phenomenon of negative adsorption inflexion (NPI) in the  $\text{CO}_2$  sorption isotherm of  $\beta$ -GS, and disclose the mechanism of  $\beta$ -GS transformation to  $\gamma$ -GS driven by  $\text{CO}_2$  uptake. Distinct from negative gas adsorption (NGA), which amplifies pressure, the NPI phenomenon enables active pressure reduction, suggesting promising applications in microscale gas regulation, such as in integrated micro-gas separators or self-regulating microfluidic components. Owing to its high  $\text{CO}_2$  uptake (Supplementary Fig. 29, Table 4), facile regeneration under mild conditions, combined with the intrinsic advantages of a solid salt, such as abundance, low cost, and high stability, GS endows it with great potential for practical  $\text{CO}_2$  capture, storage, and transport.

## Methods

### Materials

All chemicals and reagents were purchased from commercial suppliers and used without further purification. Guanidinium carbonate ( $\text{Gua}_2\text{CO}_3$ ) was purchased from Shanghai Adamas Reagent Co., Ltd. Ethanol and sulfuric acid were purchased from Sinopharm Chemical Reagent Co., Ltd. Nitrogen gas (99.999%), carbon dioxide (99.9%) and carbon dioxide-nitrogen mixture gas (30 mol%  $\text{CO}_2$  + 70 mol%  $\text{N}_2$ ) were purchased from Nanjing Special Gas Plant Co., Ltd.

### Characterizations

Thermogravimetric analyses (TGA) were performed in  $\text{N}_2$  atmosphere on a TGA Q500 integration thermal analyzer. Powder X-ray diffraction (PXRD) measurement was carried out on a Rigaku MiniFlex 600 X-ray diffractometer using  $\text{Cu K}\alpha$  radiation ( $\lambda = 1.54178 \text{ \AA}$ ). Differential Scanning Calorimetry (DSC) tests were conducted with DSC Q2000 V24.10 (Module: DSC Standard Cell RC). The gas chromatography (GC) was conducted on a Shimadzu GC-2014 gas chromatograph equipped with a CBP-PSN column and a TCD detector. Ar gas (99.999%) was used as the carrier gas. Scanning electron microscopy was carried out with a field emission scanning electron microanalyzer (Gemini SEM 500).

### Synthesis of $\alpha$ -guanidinium sulfate ( $\alpha$ -GS)

$\alpha$ -GS was synthesized according to the procedures as reported in previous work<sup>24</sup>. 18.0 g  $\text{Gua}_2\text{CO}_3$  (0.1 mol) was dissolved in 25 mL deionized water, and then dropwise added 5.4 mL concentrated  $\text{H}_2\text{SO}_4$  (98%, 0.1 mol) under stirring. The pH of the resulting solution was then adjusted to 7 with dilute  $\text{H}_2\text{SO}_4$ . In order to precipitate the product, absolute ethanol was added as an anti-solvent under constant stirring. Then the colorless powder was collected by vacuum filtration, washed with absolute ethanol, and dried at 373 K in air. Yield was calculated to be 99% based on  $\text{Gua}_2\text{CO}_3$ .

### Synthesis of $\beta$ -GS single crystals (high-temperature stable phase of guanidine sulfate)

Colorless crystals were obtained through methanol diffusion (5 mL) into  $\alpha$ -GS powder (0.18 g, 1 mmol) with subsequent static crystallization for 7 days at room temperature.

### $\text{CO}_2$ sorption measurements

Prior to adsorption measurements, the bulk powder was thoroughly ground and ball-milled to achieve a sub micron particle size, thereby minimizing the impact of intracrystalline diffusion limitations on the adsorption kinetics. An activation procedure was then conducted, wherein  $\alpha$ -GS was activated at 353 K for 8 h, while  $\beta$ -GS was treated at 453 K for 8 h. To avoid exposure to air during sample treatment, an additional *in situ* vacuum activation at a set temperature for another

2 h was performed at the site of the sample port in the adsorption instrument. Gas sorption isotherms were measured on a BEL Sorp-max instrument (BEL, Japan; detailed apparatus and mechanism illustrated in Supplementary Fig. 28). N<sub>2</sub> sorption isotherm was measured at 77 K, the equilibration conditions for each data point were set at 1% pressure fluctuance within 150 s. It was observed that the conventional equilibrium conditions did not reach equilibrium for CO<sub>2</sub> adsorption. Hence, the equilibrium time was extended for 600–3600 s. CO<sub>2</sub> sorption isotherms were measured at 298 K, with the equilibration conditions for each point set at 1% pressure fluctuance within 1800 s. Furthermore, our experiments indicate that for adsorption behavior prior to the inflection point, variations in equilibrium time have a negligible effect. Therefore, different equilibrium conditions can be applied across distinct pressure ranges to optimize data collection time, as adsorption-induced structural transitions require longer equilibration time. A preliminary study was conducted to approximate the inflection pressure range before the final experiments.

For CO<sub>2</sub> sorption isotherms at 268 K, the equilibration conditions in the range of 0.001–40 kPa were set at 1% pressure change within 600 s, while in the range of 40–100 kPa the equilibration time was set for 1800 s. For CO<sub>2</sub> sorption isotherms at 270 K, the equilibration conditions in the range of 0.001–40 kPa were set at 1% pressure change within 600 s, while in the range of 40–100 kPa the equilibration time was set for 1800 s. For CO<sub>2</sub> sorption isotherms at 273 K, the equilibration conditions in the range of 0.001–55 kPa were set at 1% pressure change within 600 s, while in the range of 55–100 kPa the equilibration time was set for 1800 s. For CO<sub>2</sub> sorption isotherms at 275 K, the equilibration conditions in the range of 0.001–60 kPa were set at 1% pressure change within 600 s, while in the range of 60–100 kPa the equilibration time was set for 1800 s. For CO<sub>2</sub> sorption isotherms at 278 K, the equilibration conditions in the range of 0.001–75 kPa were set at 1% pressure change within 600 s, while in the range of 75–100 kPa the equilibration time was set for 1800 s.

### Single-crystal X-ray diffraction (SCXRD) measurements

Single-crystal X-ray diffraction data were collected by a Rigaku Oxford Diffraction Super Nova diffractometer using Cu-K $\alpha$  radiation ( $\lambda = 1.54178 \text{ \AA}$ ) at 298 K. The data collection and processing were carried out with CrysAlisPro software. The crystal structure was solved by direct methods and refined by full-matrix least squares based on  $F^2$  using a SHELXTL 14XL program package. Hydrogen atoms were fixed geometrically at their positions and allowed to ride on parent atoms. Quantification of electron count within pores was accomplished through the SQUEEZE method<sup>37</sup> on the refinement model of the vacant framework. Details of structural analyses were summarized in Table S2. The cavity size of GS was determined using the Mercury software with a probe radius of 1.4  $\text{\AA}$ .

### Variable-temperature powder X-ray diffraction measurement on $\alpha$ -GS

Variable-temperature powder X-ray diffraction (VT-PXRD) measurements were performed on finely ground and dried  $\alpha$ -GS samples using a Rigaku MiniFlex 600 X-ray diffractometer equipped with an in-situ temperature control stage. The temperature protocol was set as follows: heating from 298 K to 473 K through incremental steps (373, 383, 403, 423, 448 and 473 K) at  $10 \text{ }^\circ\text{C min}^{-1}$ , with 3 min isothermal holds before data collection at each temperature.

### In situ powder X-ray diffraction (PXRD) patterns monitoring the phase transition from $\beta$ -GS to CO<sub>2</sub>@ $\gamma$ -GS under 100 kPa CO<sub>2</sub> at varying exposure times

The  $\alpha$ -GS powder was heated at 453 K under dynamic vacuum for 1 h to induce a complete phase transition to  $\beta$ -GS, as confirmed by PXRD. The sample was then cooled to 278 K. Under a static CO<sub>2</sub> pressure of 100 kPa at 278 K, time-dependent PXRD patterns were collected at 0, 5,

10, 20, 30, 60, 110, 140 min to monitor the structure transformation, using a Rigaku MiniFlex 600 X-ray diffractometer equipped with a pressure control system.

### PXRD of $\beta$ -GS before and after the inflection point of the adsorption isotherm at 273 K

When the adsorption pressure reaches 40 kPa (or 70 kPa), encapsulate the adsorption tube under the protection of an inert atmosphere. Then, prepare the test samples in a glove box. After that, encapsulate the silicon wafer with a transparent plastic bag that does not affect the diffraction intensity and conduct the test immediately.

### Isochoric adsorption-desorption experiments

An autoclave (30 mL) was charged with  $\beta$ -GS powder (1.0 g). The autoclave temperature was kept at 273 K using a cooling jacket. After the temperature was steady, the gas within the autoclave is evacuated using a vacuum pump and filled with 100 kPa CO<sub>2</sub>. The pressure inside the autoclave was monitored using a digital pressure meter (5 s per data point). After the adsorption was finished, as indicated by the inner pressure getting steady. The autoclave was placed in a 373 K oil bath for CO<sub>2</sub> release. To illustrate that CO<sub>2</sub> was successfully adsorbed and released, the same experiment was carried out with the same volume of NaCl instead of  $\beta$ -GS powder as a control experiment. Ten runs were conducted to evaluate the cyclic performance of CO<sub>2</sub> adsorption. After the final cycle,  $\beta$ -GS powder was heated at 373 K for 10 min, and the PXRD patterns were collected to confirm the phase stability.

### Selective adsorption of CO<sub>2</sub> in mixture gas

The selective adsorption measurement was conducted in a 250 mL autoclave charged with 0.50 g of pre-activated  $\beta$ -GS powder and maintained at 273 K using a cooling jacket. Prior to measurements, the system dead volume was calibrated using helium expansion. After temperature stabilization, the autoclave was evacuated and pressurized to 330.0 kPa with a certified gas mixture containing 70.0 mol% N<sub>2</sub> and 30.0 mol% CO<sub>2</sub>, corresponding to a CO<sub>2</sub> partial pressure of 99.0 kPa. The adsorption process continued for 24 h, with blank experiments confirming negligible background adsorption or system leakage.

Following adsorption, the solid adsorbent was transferred under argon atmosphere to a quartz bottle, where the atmosphere was replaced through five argon flush-purge cycles. The adsorbed gases were liberated by adding 5.0 mL deionized water to the solid sample under argon flow. Gas analysis was performed using a Shimadzu GC-2014 chromatograph equipped with a 5  $\text{\AA}$  molecular sieve column (2 m  $\times$  1/8 inch) and a thermal conductivity detector, using argon as carrier gas. The system calibration established a detection limit of 200 ppm for N<sub>2</sub>. Analysis of the released gas from  $\beta$ -GS samples showed N<sub>2</sub> concentrations below this detection limit, confirming the highly selective adsorption of CO<sub>2</sub> over N<sub>2</sub>.

### Validation of TGA mass loss

The theoretical mass loss is calculated as:

$$\omega_{\text{CO}_2} = \frac{n \times \text{MCO}_2}{\text{M}_{\text{host}} + n \times \text{MCO}_2}$$

host =  $\gamma$ -GS,  $n$  = the number of CO<sub>2</sub> molecules per structural unit (formula unit) (here,  $n = 4$ ).

### Computational method

**Force field level CSP.** The CSP process based on the force field was performed using the open source code mol-CSPY<sup>38</sup>. All geometries were optimized using Gaussian16 software at B3LYP/6-31 G (d,p) level of theory<sup>39</sup>, followed by frequency calculations to ensure the true local minima of the optimized structure. These molecular geometries were

held rigid throughout force field level crystal structure generation and lattice energy minimization. Trial crystal structures were generated with one guanidinium sulfate salt ( $\text{CN}_3\text{H}_6^+\cdot\text{CN}_3\text{H}_6^+\cdot\text{SO}_4^{2-}$ ) in the asymmetric unit for the following space group and generation number of trial structure: P1 (10000), P-1 (10000), P21 (20000), C2 (20000), Cc (20000), P21/c (50000), C2/c (50000), P212121 (10000), Pna21 (20000). In the mol-CSPY CSP, a quasi-random sampling method was used that all structural variables within each space group were generated from a Sobol vector: unit cell lengths and angles, and molecular positions and orientations within the asymmetric unit. Space-group symmetry was then applied, and a geometric test was performed for overlap between molecules, which was removed by lattice expansion. DMACRYS<sup>40</sup> software was used to calculate the lattice energy with an anisotropic atom–atom potential. The atomic multipole of the molecular charge distribution<sup>41</sup> based on B3LYP/6-31 G(d,p) level charge density was used to model the electrostatic interactions. Atom–atom repulsion and dispersion interactions were modeled using a revised Williams<sup>42</sup> intermolecular potential. Charge–charge, charge–dipole and dipole–dipole interactions were calculated using Ewald summation. Removal of duplicate structures was performed with the following method: all structures within a lattice energy window of 1.0 kJ mol<sup>-1</sup> and within a density window of  $\pm 0.05 \text{ g cm}^{-3}$  were compared using PXRD patterns generated by Platon<sup>43</sup> using a constrained dynamic time-warping method as implemented in the mol-CSPY.

**DFT level calculations.** After the force-field-level geometry optimization, structures within an energy window of 100 kJ mol<sup>-1</sup> above the global minimum were taken out. Duplicate structures were removed again when a 15/15 packing similarity was found within a 0.2 Å distance tolerance and a 20° angle tolerance using the CCDC API. Finally, the 2055 crystal structures, together with the two known polymorphs  $\alpha$ -GS and  $\beta$ -GS, were recalculated with the DFT method in VASP<sup>44</sup>. Projector augmented-wave (PAW) method<sup>45</sup> was applied to describe the electron–ion interactions. Generalized gradient approximation (GGA) with the Perdew–Burke–Ernzerhof (PBE) exchange correlation functional was adopted to treat electron interaction energy<sup>46</sup>. Grimme’s semi-empirical DFT-D3 scheme with Becke–Johnson damping functions was used here to give a better description of interactions<sup>47</sup>. A kinetic-energy cut-off of 600 eV was used to define the plane-wave basis set. Electronic Brillouin zone was integrated with the smallest allowed spacing between k-points (KSPACING) being 0.3/Å, and the generated grid is centered at the Gamma-point. Convergence threshold of self-consistency was set to 10<sup>-6</sup> eV during total energy and force calculation, and the Hellmann–Feynman force convergence criterion on each atom was set to smaller than 0.01 eV Å<sup>-1</sup> when geometry optimizations are needed.

**Pore-geometry analysis.** Topological analysis of the pore space within a crystal structure was performed using the void analysis tool zeo++<sup>48</sup>. The pore volume as well as pore dimension were used in this research. Probe radius of both 1.2 Å as well as 1.65 Å was used in calculations as described in the manuscript.

**Molecular dynamic method.** MD simulations were performed using the Atomic Simulation Environment (ASE) package<sup>49</sup>. The machine learning force field SevenNet-0<sup>50</sup> was used to evaluate the energy and force during the MD process. An NPT MD simulation at 273 K with a 1 fs timestep was applied, using a Nosé–Hoover thermostat<sup>51</sup> with a damping parameter of 50 timesteps and a Parrinello–Rahman barostat with a damping parameter of 75 timesteps.

**Disorder structure treat.** During the theoretical calculation, the disordered crystal structure  $\beta$ -GS was treated to remove the disordered part by the following method. Several different initial structures, each removing a different disordered part, were constructed and kept at the

highest symmetry possible. Then a DFT-level geometry optimization was performed on these structures. The crystal structure with the lowest relative lattice energy was selected to represent the non-disordered  $\beta$ -GS for the remaining calculations.

## Data availability

The authors declare that all data supporting the findings of this study are available within the paper and its Supplementary Information. The crystal structure of  $\beta$ -GS has been deposited at the Cambridge Crystallographic Data Center (CCDC) under deposition number 2463301 and can be accessed free of charge at [www.ccdc.cam.ac.uk/data\\_request/cif](http://www.ccdc.cam.ac.uk/data_request/cif). Source data for the adsorption isotherms are provided in this paper. Other data that support the findings of this study are available from the corresponding author upon request. Source data are provided with this paper.

## References

1. Datta, S. J. et al. CO<sub>2</sub> capture from humid flue gases and humid atmosphere using a microporous coppersilicate. *Science* **350**, 302–306 (2015).
2. Zhang, X.-W. et al. Tuning the gating energy barrier of a metal-organic framework for molecular sieving. *Chem.* **7**, 1006–1019 (2021).
3. Foo, M. L. et al. An adsorbate discriminatory gate effect in a flexible porous coordination polymer for selective adsorption of CO<sub>2</sub> over C<sub>2</sub>H<sub>2</sub>. *J. Am. Chem. Soc.* **138**, 3022–3030 (2016).
4. Krause, S. et al. A pressure-amplifying framework material with negative gas adsorption transitions. *Nature* **532**, 348–352 (2016).
5. Song, X. et al. Design rules of hydrogen-bonded organic frameworks with high chemical and thermal stabilities. *J. Am. Chem. Soc.* **144**, 10663–10687 (2022).
6. He, Y. et al. A microporous hydrogen-bonded organic framework for highly selective C<sub>2</sub>H<sub>2</sub>/C<sub>2</sub>H<sub>4</sub> separation at ambient temperature. *J. Am. Chem. Soc.* **133**, 14570–14573 (2011).
7. Ding, X. et al. Supramolecular polynuclear clusters sustained cubic hydrogen-bonded frameworks with octahedral cages for reversible photochromism. *Nat. Commun.* **15**, 2782 (2024).
8. Jiang, C. et al. Supramolecular entanglement in a hydrogen-bonded organic framework enables flexible-robust porosity for highly efficient purification of natural gas. *Angew. Chem. Int. Ed.* **63**, e202404734 (2024).
9. Wang, C. et al. A solution-processable porphyrin-based hydrogen-bonded organic framework for photoelectrochemical sensing of carbon dioxide. *Angew. Chem. Int. Ed.* **62**, e202311482 (2023).
10. Li, J. & Chen, B. Flexible hydrogen-bonded organic frameworks (HOFs): opportunities and challenges. *Chem. Sci.* **15**, 9874–9892 (2024).
11. Yang, Y. et al. Ethylene/ethane separation in a stable hydrogen-bonded organic framework through a gating mechanism. *Nat. Chem.* **13**, 933–939 (2021).
12. Steiner, T. The hydrogen bond in the solid state. *Angew. Chem. Int. Ed.* **41**, 48–76 (2002).
13. Xu, P. et al. Elastic ice microfibers. *Science* **373**, 187–192 (2021).
14. Liu, C. et al. Elastic hydrogen-bonded ionic framework. *Nano Res.* **16**, 10660–10665 (2023).
15. Lu, X. et al. Clathrating CO<sub>2</sub> in a supramolecular granatohedron cage with noncovalent CO<sub>2</sub>–NH<sub>3</sub> interactions and high CO<sub>2</sub> capture efficiency under ambient conditions. *ACS Appl. Mater. Interfaces* **15**, 54458–54465 (2023).
16. Manna, B. et al. Ultrahigh ionic conduction in water-stable close-packed metal–carbonate frameworks. *Inorg. Chem.* **56**, 9710–9715 (2017).
17. Wang, Y. et al. Combustible ice mimicking the behavior of a hydrogen-bonded organic framework at ambient conditions. *Nat. Commun.* **11**, 3124 (2020).

18. Song, B. Q. et al. Reversible switching between nonporous and porous phases of a new SIFSIX coordination network induced by a flexible linker ligand. *J. Am. Chem. Soc.* **142**, 6896–6901 (2020).
19. Tanaka, D. et al. Kinetic gate-opening process in a flexible porous coordination polymer. *Angew. Chem. Int. Ed.* **47**, 3914–3918 (2008).
20. Maji, T. K., Mostafa, G., Matsuda, R. & Kitagawa, S. Guest-induced asymmetry in a metal–organic porous solid with reversible single-crystal-to-single-crystal structural transformation. *J. Am. Chem. Soc.* **127**, 17152–17153 (2005).
21. Krause, S. et al. A stimuli-responsive zirconium metal–organic framework based on supermolecular design. *Angew. Chem. Int. Ed.* **55**, 1353–1357 (2016).
22. Krause, S., Hosono, N. & Kitagawa, S. Chemistry of soft porous crystals: structural dynamics and gas adsorption properties. *Angew. Chem. Int. Ed.* **59**, 15325–15341 (2020).
23. Wang, S.-S. et al. A 2D flexible cobalt-MOF: reversible solid-state structural transformation, two-step and gate-opening adsorption behaviours, and selective adsorption of C<sub>2</sub>H<sub>2</sub> over CO<sub>2</sub> and CH<sub>4</sub>. *Dalton Trans.* **52**, 8198–8203 (2023).
24. Xiang, Z. et al. Synthesis of stable single-crystalline carbon dioxide clathrate powder by pressure swing crystallization. *Cell Rep. Phys. Sci.* **4**, 101383 (2023).
25. Dera, P. K. et al. Structures of diguanidinium sulfate and guanidinium hydrogen sulfate. *Pol. J. Chem.* **74**, 1637–1644 (2000).
26. Baek, S. B. et al. High-temperature in situ crystallographic observation of reversible gas sorption in impermeable organic cages. *Proc. Natl. Acad. Sci. USA.* **112**, 14156–14161 (2015).
27. Wang, S.-M. et al. Ethane/Ethylene separations in flexible diamondoid coordination networks via an ethane-induced gate-opening mechanism. *J. Am. Chem. Soc.* **146**, 4153–4161 (2024).
28. Krause, S. et al. Negative gas adsorption transitions and pressure amplification phenomena in porous frameworks. *Chem. Soc. Rev.* **54**, 1251–1267 (2025).
29. Nyman, J. & Day, G. M. Static and lattice vibrational energy differences between polymorphs. *CrystEngComm* **17**, 5154–5165 (2015).
30. Pulido, A. et al. Functional materials discovery using energy–structure–function maps. *Nature* **543**, 657–664 (2017).
31. Zhao, C. et al. Digital navigation of energy–structure–function maps for hydrogen-bonded porous molecular crystals. *Nat. Commun.* **12**, 817 (2021).
32. Manurung, R. et al. Tunable porosity through cooperative diffusion in a multicomponent porous molecular crystal. *J. Phys. Chem. C* **119**, 22577–22586 (2015).
33. Yang, X. et al. Computational modeling and simulation of CO<sub>2</sub> capture by aqueous amines. *Chem. Rev.* **117**, 9524–9593 (2017).
34. Zhu, A.-X. et al. Tuning the gate-opening pressure in a switching PCU coordination network, X-PCU-5-Zn, by pillar-ligand substitution. *Angew. Chem. Int. Ed.* **58**, 18212–18217 (2019).
35. Dong, Q. et al. Tuning gate-opening of a flexible metal–organic framework for ternary gas sieving separation. *Angew. Chem. Int. Ed.* **59**, 22756–22762 (2020).
36. Gu, Y. et al. Soft corrugated channel with synergistic exclusive discrimination gating for CO<sub>2</sub> recognition in a gas mixture. *Nat. Commun.* **14**, 4245 (2023).
37. Spek, A. L. PLATON SQUEEZE: a tool for the calculation of the disordered solvent contribution to the calculated structure factors. *Cryst. Struct. Commun.* **71**, 9–18 (2015).
38. Case, D. H. et al. Convergence properties of crystal structure prediction by quasi-random sampling. *J. Chem. Theory Comput.* **12**, 910–924 (2016).
39. Frisch, M. et al. Gaussian 16, revision A. 03, Gaussian, Inc., Wallingford, CT. Gaussian16 (Revision A. 03) (2016).
40. Price, S. L. et al. Modelling organic crystal structures using distributed multipole and polarizability-based model intermolecular potentials. *Phys. Chem. Chem. Phys.* **12**, 8478–8490 (2010).
41. Stone, A. GDMA: a program for performing distributed multipole analysis of wave functions calculated using the Gaussian program system. (University of Cambridge, 2010).
42. Pyzer-Knapp, E. O., Thompson, H. P. & Day, G. M. An optimized intermolecular force field for hydrogen-bonded organic molecular crystals using atomic multipole electrostatics. *Struct. Sci.* **72**, 477–487 (2016).
43. Spek, A. Single-crystal structure validation with the program PLATON. *Appl. Crystallogr.* **36**, 7–13 (2003).
44. Kresse, G. & Furthmüller, J. Efficient iterative schemes for ab initio total-energy calculations using a plane-wave basis set. *Phys. Rev. B* **54**, 11169 (1996).
45. Blöchl, P. E. Projector augmented-wave method. *Phys. Rev. B* **50**, 17953 (1994).
46. Perdew, J. P. et al. Generalized gradient approximation made simple. *Phys. Rev. Lett.* **77**, 3865 (1996).
47. Grimme, S. et al. A consistent and accurate ab initio parametrization of density functional dispersion correction (DFT-D) for the 94 elements H–Pu. *J. Chem. Phys.* **132**, 154104 (2010).
48. Willems, T. F. et al. Algorithms and tools for high-throughput geometry-based analysis of crystalline porous materials. *Microporous Mesoporous Mater.* **149**, 134–141 (2012).
49. Larsen, A. H. et al. The atomic simulation environment—a Python library for working with atoms. *J. Phys.: Condens. Matter* **29**, 273002 (2017).
50. Kovács, D. P. et al. MACE-OFF: Short-range transferable machine learning force fields for organic molecules. *Nat. Commun.* **16**, 4310 (2025).
51. Nosé, S. A molecular dynamics method for simulations in the canonical ensemble. *Mol. Phys.* <https://doi.org/10.1080/00268978400101201> (1984).

## Acknowledgments

We acknowledge support from Hefei National Laboratory for Physical Sciences at the Microscale, Hefei Science Center of Chinese Academy of Sciences, Fujian Institute of Innovation of Chinese Academy of Sciences, the robotic AI-Scientist platform of Chinese Academy of Sciences, National Key Research and Development Program of China (2021YFA1500402), the National Natural Science Foundation of China (NSFC, 22471252, 21571167, 51502282 and 22075266), the Fundamental Research Funds for the Central Universities (WK2060190053 and WK2060190100).

## Author contributions

B.L. supervised the project and conceived of the idea. L.Z. and C.L. designed and carried out the experiments and analyzed the data. L.C. and C.Z. conducted theoretical calculations and assisted in data interpretation. Z.X. collected SCXRD data, solved the structure and contributed to the experimental design. C.W. performed in situ XRD measurements. S.C. conducted adsorption experiments. B.L., L.Z., and C.Z. wrote the manuscript. All authors discussed the results and assisted with the manuscript preparation.

## Competing interests

The authors declare that they have no competing interests. USTC filed one Chinese patent (application #202310841972.2) from the data reported in this study.

## Additional information

**Supplementary information** The online version contains supplementary material available at <https://doi.org/10.1038/s41467-026-69433-w>.

**Correspondence** and requests for materials should be addressed to Linjiang Chen or Bo Liu.

**Peer review information** *Nature Communications* thanks Cafer Yavuz and the other anonymous reviewer(s) for their contribution to the peer review of this work. A peer review file is available.

**Reprints and permissions information** is available at <http://www.nature.com/reprints>

**Publisher's note** Springer Nature remains neutral with regard to jurisdictional claims in published maps and institutional affiliations.

**Open Access** This article is licensed under a Creative Commons Attribution-NonCommercial-NoDerivatives 4.0 International License, which permits any non-commercial use, sharing, distribution and reproduction in any medium or format, as long as you give appropriate credit to the original author(s) and the source, provide a link to the Creative Commons licence, and indicate if you modified the licensed material. You do not have permission under this licence to share adapted material derived from this article or parts of it. The images or other third party material in this article are included in the article's Creative Commons licence, unless indicated otherwise in a credit line to the material. If material is not included in the article's Creative Commons licence and your intended use is not permitted by statutory regulation or exceeds the permitted use, you will need to obtain permission directly from the copyright holder. To view a copy of this licence, visit <http://creativecommons.org/licenses/by-nc-nd/4.0/>.

© The Author(s) 2026